



OPEN Breast imaging with ultra-low field MRI

Sheng Shen^{1,2,11}, Neha Koonjoo^{1,2,11}, Friderike K. Longarino^{3,4,5}, Leslie R. Lamb^{2,6}, Juan C. Villa Camacho^{2,6}, Torben P. P. Hornung^{1,3,7}, Stephen E. Ogier^{8,9}, Susu Yan^{2,3}, Thomas R. Bortfeld^{2,3}, Mansi A. Saksena^{2,6}, Kathryn E. Keenan^{8,12} & Matthew S. Rosen^{1,2,10,12}✉

Breast cancer screening is essential for reducing mortality, yet current modalities face significant barriers, including high costs, limited accessibility, and reliance on ionizing radiation, which leads many women to forego regular screenings. Magnetic resonance imaging (MRI) offers a radiation-free alternative, but its adoption for screening is constrained by cost, availability, and the need for IV contrast administration. In this study, we demonstrate the feasibility of ultra-low field (ULF) unilateral breast MRI for screening applications. ULF MRI was performed on 11 healthy women in a prone position. These participants were healthy women without a history of breast cancer. Three breast radiologists could reliably delineate breast outlines and distinguish fibroglandular tissue (FGT) from adipose tissue. Tissue patterns (fatty, scattered, heterogeneous, and extreme FGT) were consistently identified. In two additional patients with prior breast cancer, ULF MRI effectively eliminated magnetic susceptibility artifacts from surgical biopsy clips and in one of these patients revealed post-surgical changes following lumpectomy. Additionally, in another patient, a > 3 cm cyst, previously confirmed on standard clinical ultrasound, was feasible to visualize with ULF MRI. These findings establish the technical feasibility of ULF breast MRI. While preliminary, they motivate further technical development and evaluation to clarify its capabilities and limitations.

In 2021, over two billion women worldwide were over the age of 40^{1,2}, and each of them face the risk of developing breast cancer. This disease will affect approximately one in eight women during their lifetime³, with 85% of cases occurring in those without any family history of the disease⁴. Additionally, early-onset breast cancer tends to be more aggressive and has a poorer prognosis⁵. However, current screening guidelines are insufficient in this population^{6,7}, highlighting the need for continued advancements in early detection strategies. Currently, mammography is the most widely used imaging tool for breast cancer screening due to its accessibility and cost-effectiveness. However, it has notable limitations: it involves ionizing radiation, causes discomfort due to breast compression, has a false positive rate ranging from 10.2 to 14.4%^{8–10}, and misses 1–35% of breast cancers^{11–17}. Consequently, in the United States as of 2015, only 65.3% of women over 40 had a screening mammogram in the previous 2 years¹⁸. Given that more than half of the global population should undergo breast cancer screening multiple times in their lives¹⁹, there is an urgent need for a more accurate and patient-friendly screening tool.

Currently available MRI-based methods overcome some of these limitations²⁰, particularly in high-risk groups^{21–23}. This is because differences in soft tissues can be visualized without obfuscations from dense tissue, and MRI screening has low false-negative rates^{24,25}. MRI can detect invasive carcinomas, distinguishing between malignant and benign lesions using T1- and T2-weighted imaging with injected contrast agent enhancement²⁶. Additionally, apparent diffusion coefficient (ADC) can be used to differentiate lesions²⁷ and assess response to treatment²⁸. However, clinical breast screening exams on traditional MRI scanners require the patient to

¹Department of Radiology, A.A. Martinos Center for Biomedical Imaging, Massachusetts General Hospital, 149 13th Street, Suite 2301, Charlestown, Boston, MA 02129, USA. ²Harvard Medical School, Boston, MA 02115, USA. ³Radiation Biophysics Division, Department of Radiation Oncology, Massachusetts General Hospital, Boston, MA 02114, USA. ⁴Clinical Cooperation Unit Translational Radiation Oncology, German Cancer Research Center (DKFZ), 69120 Heidelberg, Germany. ⁵Department of Radiation Oncology, Heidelberg University Hospital, 69120 Heidelberg, Germany. ⁶Division of Breast Imaging, Massachusetts General Hospital, Boston, MA 02114, USA. ⁷Department of Physics, ETH Zürich, 8093 Zurich, Switzerland. ⁸Physical Measurement Laboratory, National Institute of Standards and Technology, Boulder, CO 80305, USA. ⁹Department of Physics, University of Colorado, Boulder, CO 80302, USA. ¹⁰Department of Physics, Harvard University, Cambridge, MA 02138, USA. ¹¹Sheng Shen and Neha Koonjoo are first authors and contributed equally to this work. ¹²Kathryn E. Keenan and Matthew S. Rosen are senior authors and contributed equally to this work. ✉email: msrosen@mgh.harvard.edu

endure a constricted setting in addition to receiving IV contrast administration. MRI as a screening modality is currently underutilized in high-risk women (defined as a lifetime risk > 20%)²⁹. While fast MRI protocols enable screening in less than 10 min³⁰, the high cost and limited number of scanners (< 38 scanners per million people in the US) prohibit their use as a primary screening tool for breast cancer.

Compared to clinical MRI systems operating at 1.5 T or 3 T, low- (< 100 mT) and ultra-low field (ULF, < 10 mT) MRI systems offer a significantly lower cost and accessible alternative with far less strict installation requirements. This accessibility opens the door to broader use, particularly in settings where traditional MRI systems are unavailable and impractical including in low- and middle-income countries globally³¹.

Low-field MRI has been successfully implemented in clinical neuroimaging, including portable 64 mT systems for bedside stroke detection^{32–34}. These systems are safe, simple to operate, and do not require specialized shielding or MRI technicians^{35,36}. Despite the inherently lower signal-to-noise ratio (SNR) at reduced field strengths, clinical efficacy has been demonstrated^{32,34,37}. Historically, nuclear magnetic resonance (NMR)-based methods have shown promise for breast imaging: T1 and T2 relaxation times of breast tissues were measured at 0.71 T³⁸ yielding encouraging results. Subsequent studies measured the T1 of mastectomy samples at 0.09 T and 0.35 T^{39,40}, and *in vivo* whole-breast imaging was attempted at 45 mT. Although these early efforts were hampered by excessively long exam times, they supported the fundamental findings of the NMR studies⁴¹. These studies demonstrated that cancerous tissues exhibit distinct T1 relaxation times from healthy fibroglandular and adipose tissue^{38,42,43}. These differences in T1 relaxation times form the basis of our current research. If we can achieve sufficient SNR within a reasonable exam duration, ULF breast MRI may enable new approaches to breast imaging, offering multi-slice soft tissue visualization beyond what is possible with the X-ray projection-based method used in mammography.

In this study, we present our preliminary evaluation of breast imaging using ULF MRI, providing an initial technical demonstration of *in vivo* breast imaging at 6.5 mT. Utilizing a laboratory-based ULF MRI system operating at 6.5 mT with a unilateral conical RF coil (see Fig. 1), we imaged the left breasts of 11 healthy women, who were participants without a history of breast cancer. Separately, we scanned two patients with a history of breast cancer (one right and one left breast) to evaluate post-surgical changes, and one additional patient was imaged with a known benign mass on the left breast. In healthy participants, the ULF MR images of the whole breast revealed essential breast features, including type of fibroglandular tissue (FGT), breast outline, nipple areolar complex (NAC), and chest wall. Additionally, for three healthy participants the 3D ULF MRI scans are compared to their X-ray mammogram. For both patients with a history of breast cancer, the artifacts typically generated by surgical clips and post-surgical changes were evaluated. And lastly, the feasibility of detecting a benign mass at ULF was also investigated.

Results

Participant characteristics and imaging protocol

ULF MRI was used to image the left breast of 11 healthy women (mean age, 35 years \pm 13 years), who were without history of breast cancer. Additionally, three patients participated: a 51-year-old patient with a history of invasive ductal carcinoma (grade 1) and papillary carcinoma (grade 1), a 58-year-old patient with a history of invasive lobular carcinoma (grade 3), and a 48-year-old patient with a known benign mass. All women completed the study.

A 3D balanced SSFP (bSSFP) sequence was used with a constant voxel size of 3 mm \times 3 mm \times 8 mm, and the resulting total scan time was 21 min 36 s for all the healthy participants. For the three cases with known pathology, a higher spatial resolution was used depending on the breast size. For larger breast size ($n=1$), a 30-min scan with a voxel size of 2 mm \times 2 mm \times 6 mm was used, and for smaller breast size ($n=2$), a 45-min scan with a voxel size of 2 mm \times 2 mm \times 4 mm was used. No data-driven Artificial Intelligence (AI) or other machine learning-based methods were used in the image acquisition or reconstruction.

The MR sequence and positioning were well tolerated. None of the images were degraded by patient motion. It is noteworthy that none of the participants experienced discomfort during the exam, and the breast fit naturally in the conical-shaped RF coil without compression.

ULF MRI breast imaging findings

Image sets of the entire left breast for three representative subjects with different breast tissue patterns are shown in Figs. 2, 3 and 4. For these three representative subjects, the following features were labeled by a breast radiologist: visibility of the breast outline, NAC, FGT and chest wall. The bSSFP pulse sequence has a mixed contrast that depends on the ratio of T2/T1, such that fat tissue appears bright and fibroglandular tissue appears dark.

Breast images from all 11 participants were evaluated by three independent board-certified breast radiologists for the purpose of categorizing breast density and assessing the visibility of essential breast tissues, which include the type of FGT, the breast outline, the NAC, and the chest wall. Individual image scores are reported in Table 1. Breast tissue pattern was assessed using fatty, scattered FGT, heterogeneous FGT, and extreme FGT. Inter-reader reliability of breast tissue pattern was determined using Fleiss' kappa, which resulted in a kappa value of 0.73 (95% confidence interval 0.72–0.74, $p < 0.001$), indicating substantial agreement among the readers.

Visibility of the following features in the breast was scored using a 5-point Likert scale (1—not at all visible to 5—clearly visible and very sharp): breast outline, FGT compared to intramammary adipose tissue, demarcation of the NAC, and the chest wall, defined as visualization of the pectoralis muscle. The limited data set from this pilot study did not allow for proper training of the readers, and given the novelty of the images, the readers were not well “calibrated” to each other. For example, when evaluating the visibility of the breast outline, we find the readers were internally consistent: each reader scores all images with the same visibility (with the exception of a single case for reader 1 that received a higher score). However, each reader has assigned a different visibility

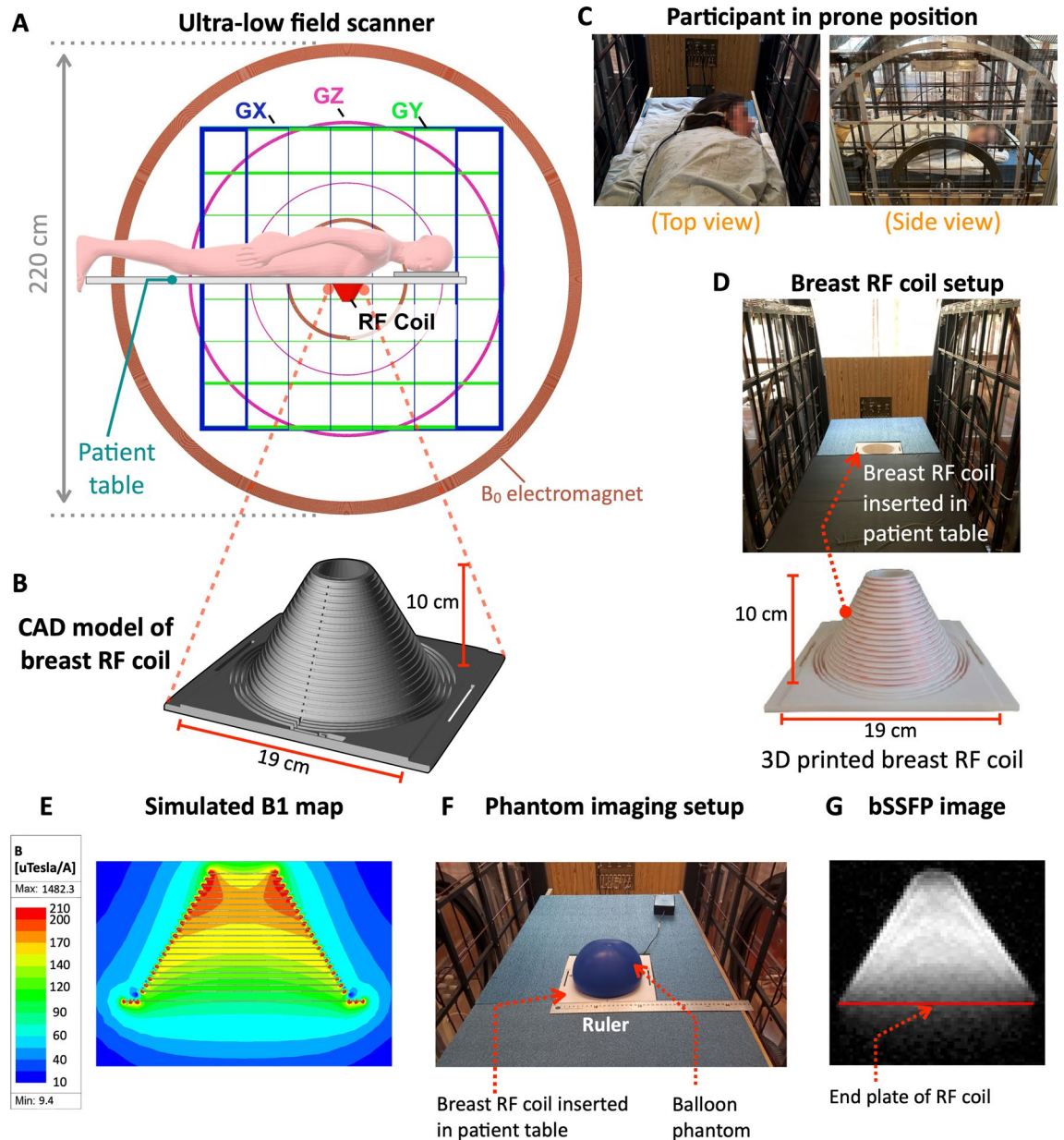


Fig. 1. 6.5 mT ULF MRI scanner configured for breast imaging—(A) Axial view of the ULF MRI scanner. The three axes of the gradient set are shown as Gx (in blue), Gy (in green) and Gz (in magenta), and the biplanar coils of the resistive electromagnet are shown in brown (two per side, four total). The participant lays on the patient table in the prone position with the head turned to the side. The breast is placed in the RF coil located at the scanner isocenter. (B) CAD model of RF coil designed for breast imaging at 276 kHz. *In vivo* experimental setup—(C) The top and side view of the subject lying in the prone position on the subject table with the breast placed into the RF coil. (D) A view of the subject table with red arrow indicating the location of the 3D printed breast RF coil fixed. Assessment of the imaging volume of the conical-shaped breast RF coil. (E) The magnetic field calculation of the breast RF coil where the color bar indicates the B1 field distribution (in $\mu\text{T}/\text{A}$) across the breast volume. (F) A homogeneous phantom was imaged with a latex balloon (blue) filled with ionized water placed inside the breast RF coil. (G) Central slice of a 21-slice 3D-bSSFP acquisition of the balloon phantom. The scan shows the signal uniformity of the RF coil. The red line indicates the end of the plate of the RF coil.

score from the other readers. As a result, a binary rating system was adopted from the 5-point scale with a score of 1 remaining not at all visible and scores 2–5 as visible. Fleiss' kappa was also used to measure the agreement regarding the visibility of essential breast tissues which included the type of fibroglandular tissue, the breast outline, NAC, and the chest wall. In this binary framework, consensus on the visibility of the breast outline and FGT was consistent ($\text{kappa} = 1$), whereas the NAC and chest wall exhibited kappa values of 0.54 (95% confidence interval 0.58–0.60, $p < 0.001$) and 0.27 (95% confidence interval 0.26–0.28, $p < 0.2$), respectively.

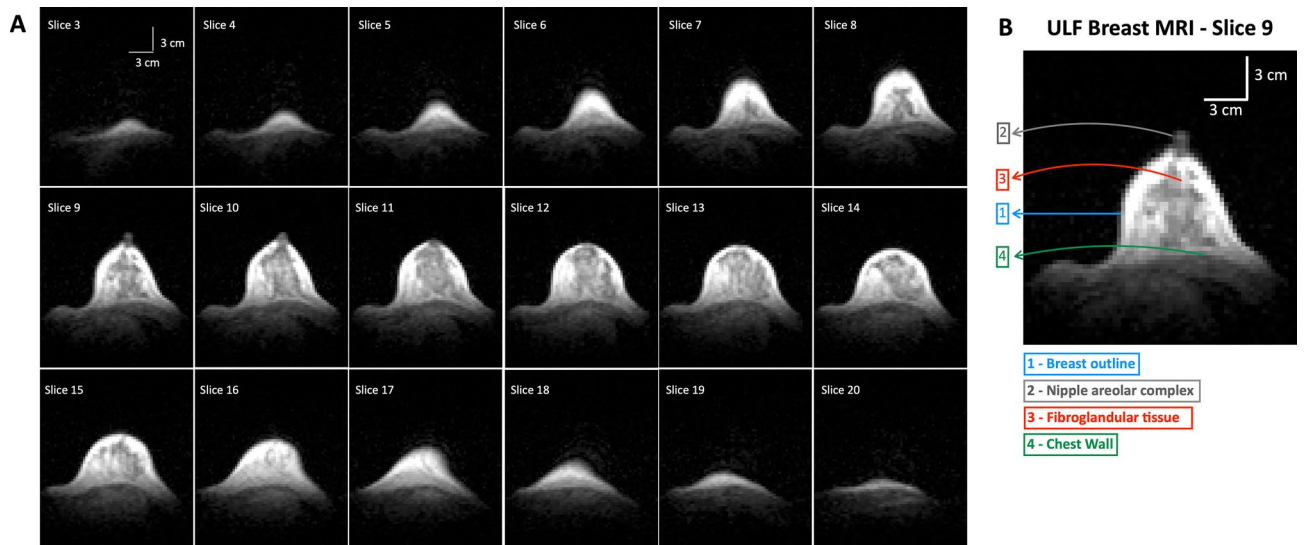


Fig. 2. 3D ultra-low field breast MRI obtained at 6.5 mT from a 34-year-old healthy woman with heterogeneous fibroglandular tissue (FGT). **(A)** 18 out of 21 sequential axial bSSFP-weighted slices of the left breast are shown, and no contrast agent was administered. Data was acquired in approximately 21 min with a spatial resolution of $3\text{ mm} \times 3\text{ mm} \times 8\text{ mm}$. Vertical and horizontal scale bars in white are 3 cm each and are shown in slice 3. **(B)** A representative axial slice is shown, where all features are visualized in this study: breast outline, FGT, nipple areolar complex, and chest wall.

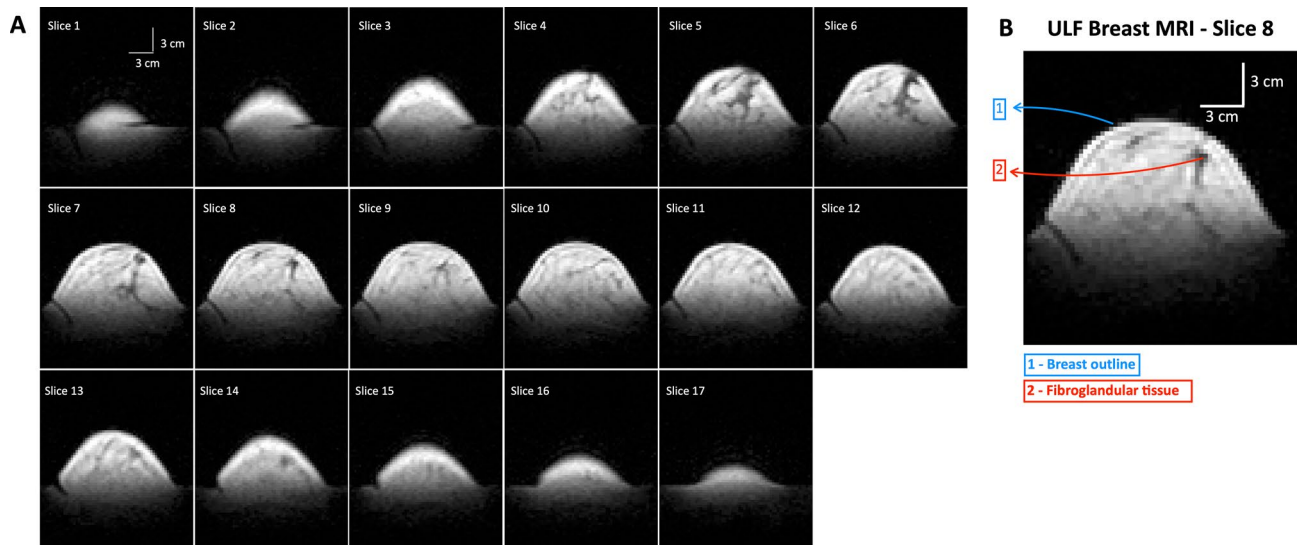


Fig. 3. 3D ultra-low field breast MRI obtained at 6.5 mT from a 31-year-old healthy woman with scattered fibroglandular tissue (FGT). **(A)** 17 out of 21 representative sequential axial bSSFP-weighted slices of the left breast are shown, and no contrast agent was administered. Data was acquired in approximately 21 min with a spatial resolution of $3\text{ mm} \times 3\text{ mm} \times 8\text{ mm}$. Vertical and horizontal scale bars in white are 3 cm each and are shown in slice 1. **(B)** The nipple areolar complex and chest wall were not well visualized in this study. In the representative slice 8 shown, the breast outline and FGT were visualized and annotated by a breast radiologist.

ULF MRI acquisition and X-ray mammography of healthy participants

Three of the 11 healthy participants had a bilateral screening mammogram within 8 months of their participation in the ULF MRI study. These mammograms were labelled by a breast radiologist with 13 years of experience. All three participants have scattered fibroglandular tissue, and Fig. 5 shows a representative case with the different breast features identified on both the ULF MRI and the mammogram. The other two cases are reported in Figs. S1 and S2 in the supplemental material. Comparison to mammography confirms that the ULF MRI reliably shows the fibroglandular tissue.

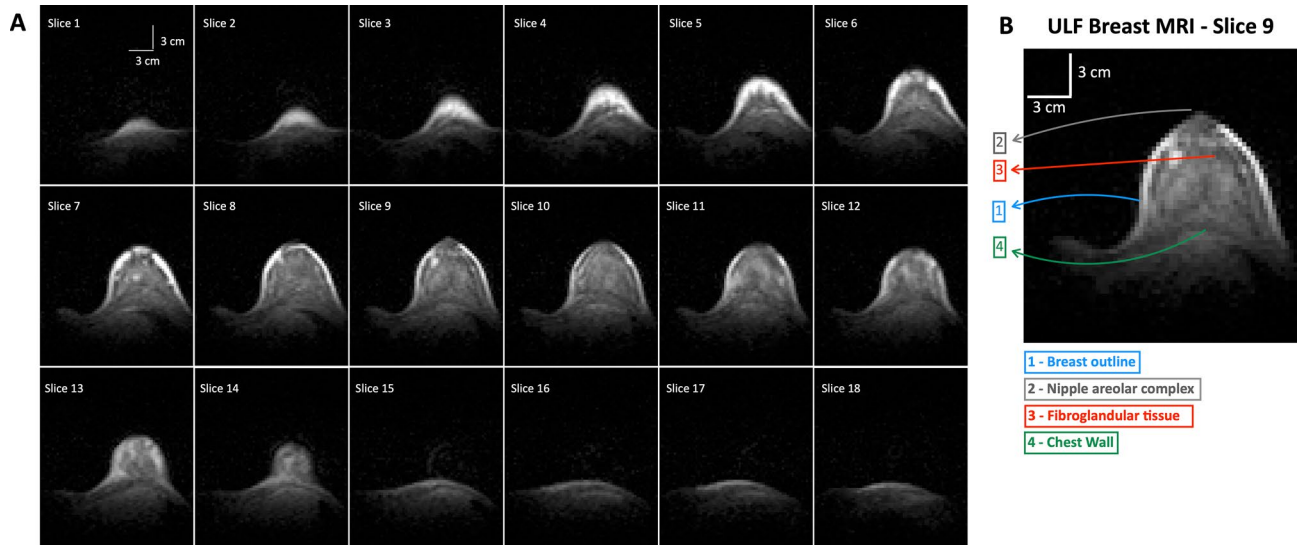


Fig. 4. 3D ultra-low field breast MRI obtained at 6.5 mT from a 31-year-old healthy woman with extreme fibroglandular tissue (FGT). **(A)** 18 out of 21 representative sequential axial bSSFP-weighted images of the left breast are represented. No contrast agent was administered. Data was acquired in approximately 21 min with a spatial resolution of 3 mm × 3 mm × 8 mm. Vertical and horizontal scale bars in white are 3 cm each and are shown in slice 1. **(B)** A representative slice was labelled by a breast radiologist, and all features are visualized in this study: breast outline, FGT, nipple areolar complex, and chest wall.

| Feature | Reader # | Subject # | | | | | | | | | | | Statistical Analysis | |
|-----------------------------------|----------|-----------|--------|--------|--------|--------|--------|--------|--------|--------|---------|---------|------------------------------|---------|
| | | Subj 1 | Subj 2 | Subj 3 | Subj 4 | Subj 5 | Subj 6 | Subj 7 | Subj 8 | Subj 9 | Subj 10 | Subj 11 | Fleiss Kappa test | |
| | | | | | | | | | | | | | kappa (95% confidence level) | p value |
| Breast tissue pattern | 1 | B | C | B | C | B | D | C | C | B | C | D | 0.73 * (0.72 – 0.74) | <0.001* |
| | 2 | B | C | B | C | B | D | C | C | B | C | D | | |
| | 3 | A | C | A | B | B | D | C | C | B | C | D | | |
| Breast outline visibility | 1 | 4 | 4 | 4 | 4 | 5 | 4 | 4 | 4 | 4 | 4 | 4 | 1 | - |
| | 2 | 3 | 3 | 3 | 3 | 3 | 3 | 3 | 3 | 3 | 3 | 3 | | |
| | 3 | 5 | 5 | 5 | 5 | 5 | 5 | 5 | 5 | 5 | 5 | 5 | | |
| Fibroglandular tissue visibility | 1 | 3 | 3 | 3 | 3 | 3 | 3 | 3 | 3 | 3 | 3 | 3 | 1 | - |
| | 2 | 2 | 3 | 2 | 3 | 2 | 2 | 2 | 3 | 2 | 3 | 3 | | |
| | 3 | 3 | 3 | 3 | 3 | 3 | 3 | 3 | 3 | 3 | 3 | 3 | | |
| Nipple Areolar Complex visibility | 1 | 3 | 4 | 1 | 3 | 1 | 4 | 4 | 3 | 1 | 3 | 3 | 0.54 (0.58 – 0.6) | <0.001 |
| | 2 | 2 | 3 | 1 | 2 | 2 | 3 | 3 | 2 | 1 | 3 | 3 | | |
| | 3 | 2 | 4 | 1 | 3 | 2 | 3 | 4 | 3 | 2 | 4 | 4 | | |
| Chest wall visibility | 1 | 3 | 4 | 4 | 4 | 1 | 4 | 3 | 4 | 4 | 4 | 3 | 0.27 (0.26 – 0.28) | <0.2 |
| | 2 | 1 | 2 | 2 | 2 | 1 | 2 | 2 | 2 | 2 | 2 | 2 | | |
| | 3 | 3 | 4 | 4 | 4 | 3 | 3 | 4 | 3 | 4 | 3 | 2 | | |

Table 1. Qualitative assessment of imaging in the 11 healthy subjects. Three breast radiologists assessed each imaging feature on a 5-point Likert scale of 1–5 (1—not at all visible, 2—barely visible, 3—clearly visible but blurred, 4—clearly visible and sharp, 5—clearly visible and very sharp). Breast tissue pattern (density) was evaluated using A—Fatty, B—Scattered FGT, C—Heterogenous FGT, and D—Extreme FGT. Subj Subject. *The Fleiss kappa test on the breast tissue pattern was based on a 4-level score: 1- F, 2- S, 3- S and 4-E. Inter-reader analysis on the 4 remaining imaging features were assessed on as a binary rating system, where scores of 2–5 were categorized as visible and a score of 1 as not visible.

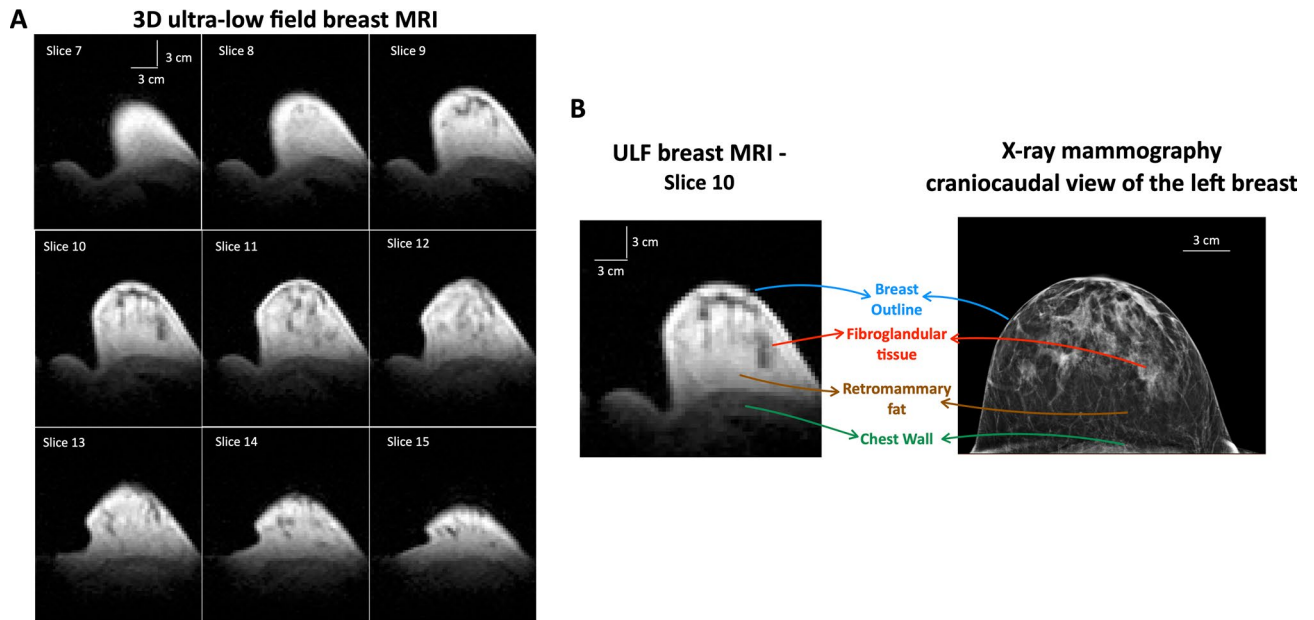


Fig. 5. 3D ultra-low field breast MRI obtained at 6.5 mT and X-ray mammogram of a 48-year-old healthy woman with scattered fibroglandular tissue (FGT). **(A)** 9 out of 21 representative sequential axial bSSFP-weighted images of the left breast are shown. No contrast agent was administered. Data was acquired in approximately 21 min with a spatial resolution of 3 mm × 3 mm × 8 mm. Vertical and horizontal scale bars in white are 3 cm each and are shown in slice 7. **(B)** Slice 10 is a representative slice of the ULF scan, labelled by a breast radiologist, where breast outline, fibroglandular tissue, retromammary fat, and chest wall were visualized. The craniocaudal view of the X-ray mammogram is shown alongside the breast radiologist's labels. The same four breast features were also identified on the mammogram. Vertical and horizontal scale bars in white are 3 cm each. Images were reconstructed without the use of AI or ML-based approaches.

Patient scanning at ULF MRI

Imaging was also performed in three patients with a history of breast disease: two with a history of breast cancer and one with a palpable, known cystic mass. For these studies, the spatial resolution was increased in all three dimensions, and to maintain SNR, signal averaging was increased resulting in a longer scan time.

Figure 6 shows the images of a patient with a history of invasive ductal carcinoma (grade 1) and papillary carcinoma (grade 1) in the subareolar region of the right breast diagnosed 2 years prior to this study. The patient received a localized lumpectomy prior to tamoxifen treatment. The ULF MRI showed all breast features including NAC, breast outline, FGT, retromammary fat, and chest wall. ULF MRI also depicted the linear vertical hypointense post-surgical change at the site of the lumpectomy, corresponding to the same linear hypointense scar tissue seen on the 3 T MRI. In comparison, the X-ray mammogram and the 3 T clinical breast MRI also showed the different breast features. The mammogram clearly visualized the surgical clips, and the expected clip-related susceptibility artifacts were visible on the 3 T MRI scan. These susceptibility artifacts were not seen on the ULF MRI scan.

Figure 7 shows representative slices of a patient with a history of invasive lobular carcinoma (grade 3) in the left breast. The patient received a lumpectomy 3 years prior to this study. The surgical clips were not visible on ULF images due to their small size (length 4 mm) and due to the absence of susceptibility artifacts at lower magnetic field strengths. The surgical clips are visible on X-ray mammogram, and at 3 T MRI, the susceptibility artifacts indirectly show the location of the surgical clips.

Figure 8 shows images from a patient with a palpable mass that was imaged with ULF MRI; the patient had a known cystic mass on X-ray mammogram and on the targeted ultrasound exam. On ULF MRI, the cystic mass is clearly visible on five slices at approximately 1 cm above the nipple on the medial side of the left breast. The location of the mass was confirmed by a breast radiologist. Using ULF MRI, the size of the mass was evaluated as 33 mm × 20 mm × 18 mm, which agrees with the reported values assessed on the ultrasound exam of 35 mm × 26 mm × 16 mm. The volume of the mass estimated using the 3D ULF MRI was 8.16 cm³.

Discussion

In this preliminary study, we successfully performed *in vivo* MR breast imaging at 6.5 mT on healthy participants and three patients, including two with a history of breast cancer and one with a benign cystic mass. Essential breast features were identified such as breast outline, FGT, NAC, and chest wall. We included 11 participants with a range of breast sizes, and images were acquired using a single bSSFP sequence with an imaging duration of approximately 21 min for healthy participants. The three clinical case studies included two patients with a history of breast cancer who have both undergone lumpectomy and one patient with a known > 3 cm benign simple cyst. All of the ULF MRI scans were acquired at 6.5 mT without the use of exogenous IV contrast agents

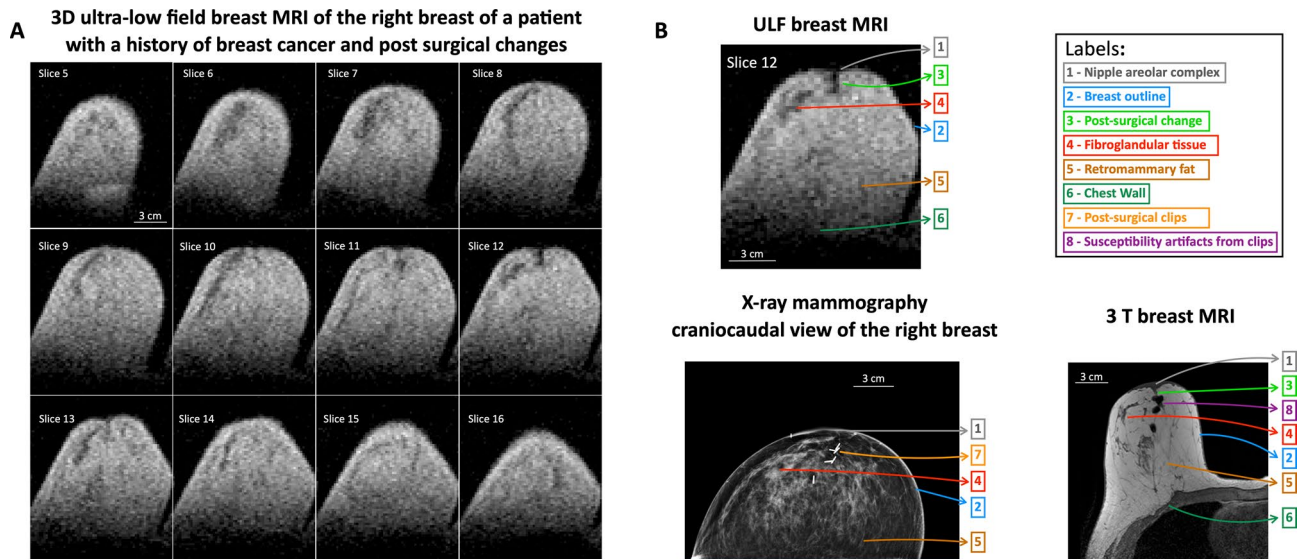


Fig. 6. Observation of post-surgical changes on a 3D ultra-low field breast MRI scan of the right breast of a 51-year-old woman diagnosed 2 years prior to this study with invasive ductal carcinoma (grade 1) and papillary carcinoma (grade 1) in the subareolar region of the right breast. Patient received a localized lumpectomy prior to tamoxifen treatment. **(A)** 12 out of 21 representative sequential axial bSSFP-weighted images of the right breast are shown. No contrast agent was administered. Data was acquired in approximately 30 min with a spatial resolution of $2\text{ mm} \times 2\text{ mm} \times 6\text{ mm}$. **(B)** A representative slice, slice 12 of the 3D ULF scan, the craniocaudal view of the mammogram of the right breast and the corresponding slice of the 3 T MRI scan of the right breast were labelled by a breast radiologist. The radiologist labelled the breast tissue pattern as scattered fibroglandular tissue (FGT), and the features visualized in this study were: breast outline, nipple areolar complex, FGT, retromammary fat, and chest wall. The linear hypointense scar tissue was detected on the ULF scan corresponding to same hypointense post-surgical change on the 3 T scan; no susceptibility artifacts from the surgical clips were observed. The surgical clips were all visible on the mammogram. On the high field MRI scan, the susceptibility artifacts from the surgical clips were visible. Horizontal scale bars in white are 3 cm.

or the use of machine learning for image acquisition and reconstruction. These promising results motivate us to further develop ULF MRI for breast imaging.

Globally, one-eighth of the population, or 2.2 billion women over age 40, are recommended to undergo regular breast cancer screenings⁴⁴. This translates to approximately 500 million screening exams needed every year, vastly surpassing the combined total of head injuries, strokes and brain tumors, which are estimated as 85 million annually^{45–48}. While ULF MRI is far from meeting clinical requirements, the substantial scale of breast imaging motivates continued exploration of technologies that could, in the long term, broaden the range of available imaging approaches. Our current study provides an initial technical foundation for such future investigations.

MRI at low- and ultra-low magnetic fields is challenging due to inherently low Boltzmann polarization and consequently low signal. Two additional consequences of MRI physics at ultra-low magnetic field are relevant to this work. First, as magnetic field decreases, tissue T1 relaxation times generally decrease, while T2 relaxation times are generally constant across fields^{42,49}. Second, the magnetic susceptibility artifacts are significantly reduced at ULF. We leverage both of these aspects to our advantage at 6.5 mT, where the efficiency of bSSFP in this regime is maximal⁵⁰ and enables banding-free imaging over large fields of view. In this study, the image SNR was sufficient to visualize key breast tissues.

The three expert readers had substantial agreement in their evaluations of breast tissue patterns and key breast tissues. However, there were notable discrepancies: Reader 2's scores were, on average, 33% lower than those of Reader 1 (paired t-test, $p < 0.001$) and 28% lower than Reader 3 (paired t-test, $p < 0.001$). Additionally, Reader 3's scores were 7.01% higher than those of Reader 1 (paired t-test, $p < 0.03$). There was also some disagreement regarding the visibility of the NAC and chest wall.

These discrepancies can be attributed primarily to the novelty of ULF MRI for the readers rather than intrinsic difficulty in identifying key breast anatomy. While structures such as the NAC and chest wall are readily visible on standard 1.5 T and 3 T clinical breast MRI, their appearance on ULF images was less familiar, contributing to variability in scoring. Additionally, the limited dataset prevented extensive hands-on calibration, and the evaluation criteria were discussed but not practiced prior to scoring. In contrast, when evaluating clinical breast MRI scans, the readers are implicitly calibrated, having each examined numerous scans over extensive periods (13 years, 3 years and 9 years, respectively). This experience gap underscores the need for dedicated training and calibration when introducing new imaging technologies like ULF MRI to ensure accurate and consistent evaluations. Future studies with larger multi-reader datasets may enable a more detailed evaluation of inter-

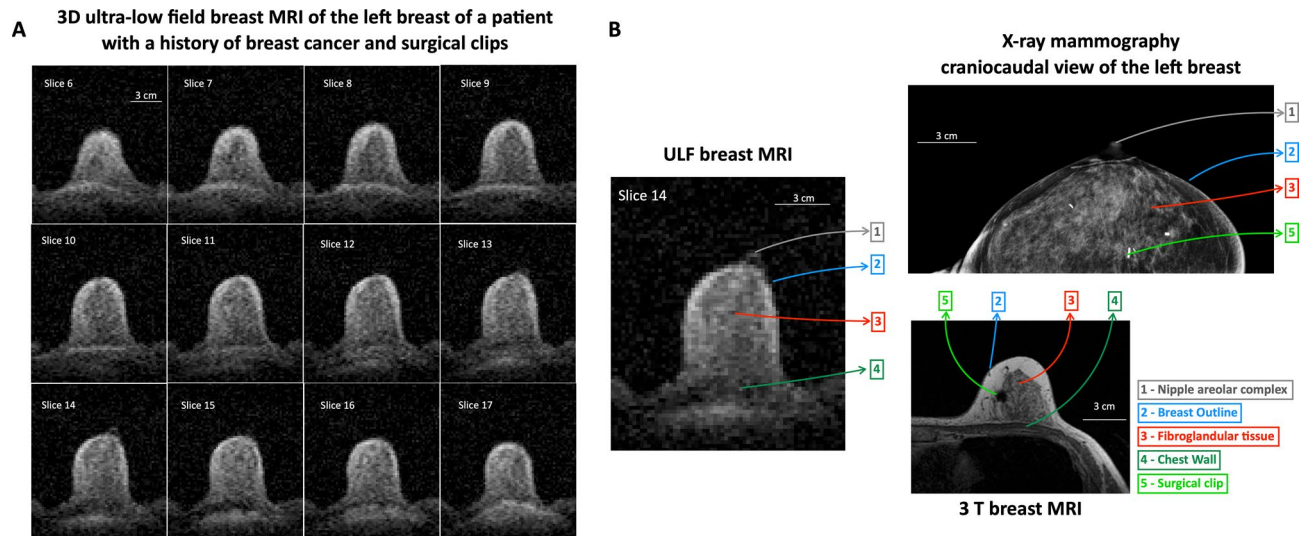


Fig. 7. Example of reduction of susceptibility artifacts from surgical clips on a 3D ultra-low field breast MRI scan of the left breast of a 58-year-old woman diagnosed 3 years prior to this study with invasive lobular carcinoma (grade 3). Patient received a left breast lumpectomy. **(A)** 12 out of 21 representative sequential axial bSSFP-weighted images of the left breast are shown. No susceptibility artifacts were seen on the ULF MRI. No contrast agent was administered. Data was acquired in approximately 45 min with a spatial resolution of $2\text{ mm} \times 2\text{ mm} \times 4\text{ mm}$. **(B)** A representative slice, slice 14, was labelled by a breast radiologist, where the following features were visualized: nipple areolar complex, breast outline, FGT, and chest wall. The breast tissue is heterogeneously dense. The craniocaudal view of the mammogram showed the nipple areolar complex, the breast outline, the fibroglandular tissue, and the surgical clips. The 3 T bilateral breast MRI image showed the breast outline, the fibroglandular tissue, the chest tissue, and the susceptibility artifact from the surgical clip at the site of the lumpectomy. Horizontal scale bars in white are 3 cm.

observer variability, which was beyond the scope of the current work but represents an important direction for future research.

The visibility of the NAC and chest wall was inconsistent across scans. The absence of the NAC in certain images may be attributed to slice thickness, breast positioning, or natural anatomical variations such as flat or inverted nipples. The chest wall was not always visible, primarily in participants with a larger breast. This is a limitation of the RF coil design: with an imaging depth of approximately 3 cm from the coil's end plate, the chest wall was not fully captured in individuals with larger breast sizes. This design constraint highlights a significant area for improvement in coil development to enhance imaging coverage for diverse breast sizes.

For three of the healthy participants, recent mammograms were available. The comparison between ULF MRI scan and its corresponding mammogram shows that ULF MRI can determine fibroglandular tissue pattern and all four essential breast features. In the future, ULF MRI should be compared with mammography of participants with different breast tissue pattern (e.g., dense fibroglandular tissue). When available, digital breast tomosynthesis (DBT) was reviewed for comparison with ULF MRI in the healthy participants. In this cohort, DBT appeared similar to 2D mammography and did not provide additional value. However, since DBT is clinically most useful for the detection of subtle architectural distortions and small masses, future studies including patients with such findings will enable a more meaningful comparison between DBT and ULF MRI.

Post-surgical changes were observable on ULF MRI scans for the patient diagnosed 2 years prior to this study with invasive ductal carcinoma (grade 1) and papillary carcinoma (grade 1) in the subareolar region of the right breast. While partial volume effects due to the 6 mm slice thickness could theoretically obscure some clips, the presence of multiple clips at different superior-inferior levels makes it unlikely that all clips would be missed. Unlike at 1.5 T or 3 T, these changes were not obscured by susceptibility artifacts from surgical clips. In contrast, the location of surgical clips were not observed for the patient diagnosed 3 years prior to this study with invasive lobular carcinoma (grade 3). Typically, surgical clips are placed during biopsy or surgical procedures to serve as localization markers. On high-field breast MRI (1.5 T or 3 T), these clips generate susceptibility artifacts visible as dark patterns larger than the clips, which aid in locating the clips but also obscure the surrounding breast tissue. In ULF MRI, susceptibility artifacts from surgical clips are absent, allowing for unobstructed imaging of breast tissue. However, this lack of artifacts also makes it more challenging to locate the surgical clips themselves. To date, the scientific evidence on whether these susceptibility-related image artifacts in breast MRI may lead to misinterpretations or the inability to detect the respective lesion is very limited^{51,52}. However, if low field breast MRI becomes a screening technique, the absence or reduced susceptibility artifacts caused by metallic marking clips may become relevant in future evaluations of ULF MRI performance in patients who have retained tissue marker clips or foreign bodies within the breast tissue.

At ULF, the cystic mass that was already proven on ultrasound was easily detected on multiple slices of the MR image. The bright MRI signal on the bSSFP scan and the dark signal on ultrasound indicate that the benign

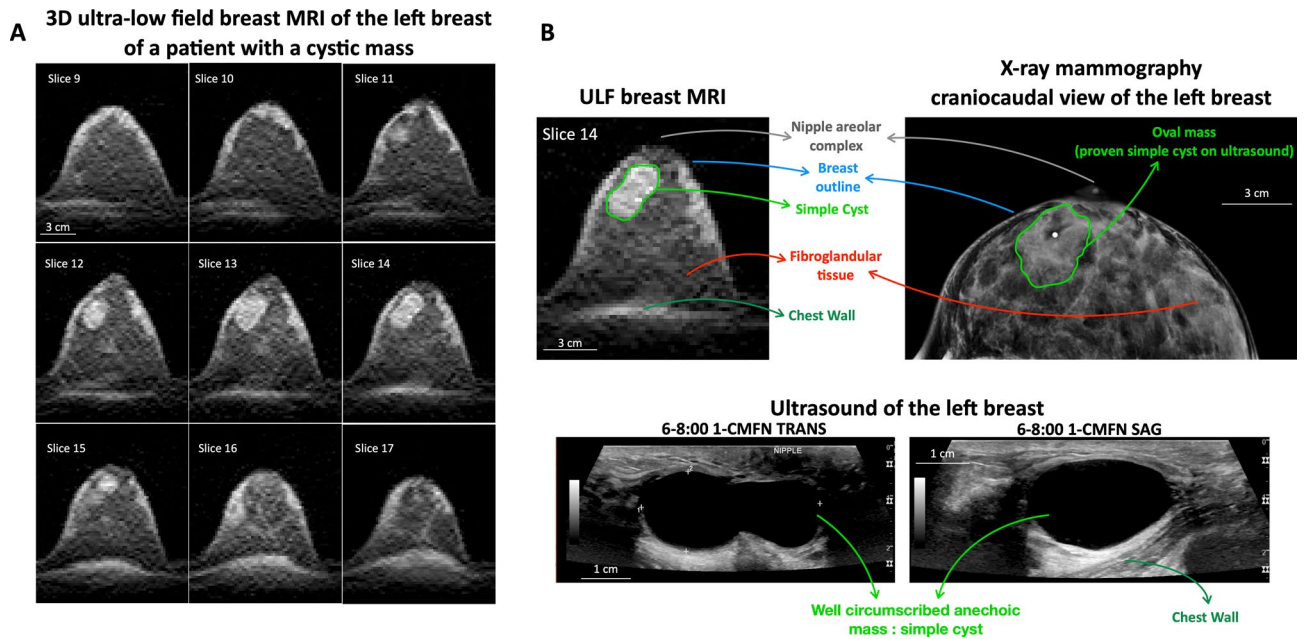


Fig. 8. Observation of a known mass on a 3D ultra-low field breast MRI scan of a 48-year-old woman in the subareolar region of the left breast near the nipple. Patient received an X-ray mammogram and a targeted breast ultrasound, which confirmed a benign cystic mass. (A) 9 out of 21 representative sequential axial bSSFP-weighted images of the left breast are shown. No contrast agent was administered. The cystic mass was detected on the ULF scan on several slices. The breast radiologist confirmed its location. Data was acquired in approximately 45 min with a spatial resolution of $2\text{ mm} \times 2\text{ mm} \times 4\text{ mm}$. (B) A representative slice, slice 14 was labelled by a breast radiologist, where the features visualized in this study were: breast outline, FGT, nipple areolar complex, chest wall, and the oval mass. The breast tissue is extremely dense. The craniocaudal view of the mammogram showed breast outline, FGT, nipple areolar complex, and the oval mass. The targeted ultrasound exam of the left breast revealed a bilobular anechoic mass with the reported dimensions of $35\text{ mm} \times 26\text{ mm} \times 16\text{ mm}$. The cystic mass was segmented on the ULF scan, and the dimensions of the mass was determined to be $33\text{ mm} \times 20\text{ mm} \times 18\text{ mm}$ (volume = 8160 mm^3). Horizontal scale bars in white are 3 cm.

mass is fluid-filled. In contrast, X-ray mammography cannot differentiate between tissue types and is limited to detecting density variations. Based on the visibility of fibroglandular tissue in our dataset, our breast radiologist was able to identify structures with an apparent size down to approximately 5 mm in-plane. While this suggests that cystic lesions of comparable size could be detectable under our current protocol, this represents an estimate derived from visual assessment rather than a systematic evaluation of lesion detectability. In ultra-low magnetic field imaging, a bSSFP sequence produces bright signals for both fatty tissues and fluids, which is a limitation of the current approach. This overlap prevents distinction between fat and fluid without additional imaging techniques. It is worth noting that our study relied solely on bSSFP acquisitions. Other sequence types, such as diffusion-weighted imaging (DWI), may hold potential to provide complementary diagnostic information at ULF. However, implementing DWI at such low fields is technically challenging due to reduced SNR, limited gradient performance, and increased sensitivity to motion. While not addressed in the present study, investigating whether optimized DWI strategies can be successfully adapted to ULF represents an important area for future research.

Our current study faces several limitations. We were limited by the small cohort and lack of patients with malignant lesions, suspected recurrence, or additional benign lesions. Recruitment of these patient groups in future studies will be essential to rigorously evaluate the diagnostic potential of ULF MRI. Eight out of eleven healthy subjects did not have a mammogram or clinical breast MRI for comparison. This is because those participants belonged to a younger age group who have not yet undergone breast screening. Hence, to facilitate evaluation, our three breast radiologists leveraged their expertise in interpreting clinical breast MRI scans. Nevertheless, this exploratory phase provided valuable insights into the potential of ULF imaging, paving the way for future refinement and standardization. Besides the issue of incomplete visualization of the chest wall, our preliminary study did not image the axilla, a crucial area for detecting breast cancers and nodal disease. Furthermore, a lower spatial resolution of $3\text{ mm} \times 3\text{ mm} \times 8\text{ mm}$ was applied to the 11 healthy participants to demonstrate the potential of ultra-low field breast MRI to clinicians while ensuring a reasonable scan time. The image resolution used for scanning the 11 healthy participants does not meet clinical standards for breast cancer screening, which require a spatial resolution of approximately $1\text{ mm} \times 1\text{ mm} \times 3\text{ mm}$ ⁵³ to effectively detect small tumors. Although higher spatial resolution was performed in three patients, this came at the cost of longer scan times. Notably, the 3D ULF MRI images allowed precise measurement of the cyst volume in the left breast of

the patient with a benign mass. Ideally, both breasts and axilla should be imaged simultaneously at this target resolution within a 10-min scan.

Our current results highlight that chest wall visibility and imaging depth were limited by the RF coil design. Similar challenges have been reported in low-field breast coil development^{54,55}. Future iterations of coil design, building on these established approaches, should aim to extend the field of view to include the chest wall and axilla while accommodating a range of breast sizes as it would significantly reduce total exam time and bring us closer to meeting the clinical resolution requirements. Furthermore, it will be crucial to develop a dual-coil system to enable simultaneous imaging of both breasts. Coil decoupling strategies, including geometric overlap and low-input impedance preamplifiers, will be implemented to minimize cross-talk between the coils. Additionally, multi-channel receive coils and parallel imaging techniques will be explored to accelerate acquisition, maintain high SNR across the expanded field-of-view, and keep scan times within clinically acceptable limits.

The work presented here was acquired on our 6.5 mT ULF MRI system which is a configurable test bed system developed in our laboratory to perform preliminary research and optimization of breast cancer imaging techniques. For clinical applicability, enhancing the SNR is crucial, as it can be used to attain higher resolution, shorter scan time, or both. While our current results are based on a 6.5 mT system, operating at even moderately higher magnetic fields (B_0) would significantly improve performance, given that under idealized conditions, the SNR is proportional to $B_0^{3/2}$ ⁵⁶. Thus, increasing the field strength beyond 6.5 mT has the potential to enhance SNR, enabling higher resolution imaging or shorter scan durations.

At 1.5 T and 3 T, chemical-shift fat suppression is a necessary part of breast imaging. We note that the absolute chemical shift between fat and water decreases with decreasing field strength, making conventional fat suppression techniques more challenging. Previous work using NMR and NMR dispersion techniques observe that the T1 relaxation time of adipose tissue in the breast does not change with field strength, while the T1 relaxation time of fibroglandular tissues do change with field strength^{42,43}. Thus, it may be possible to make a fat suppression technique that takes advantage of the T1 relaxation time differences with field strength (i.e., T1 dispersion).

With this perspective on low-field MRI physics, our initial results suggest several directions for future technical development of ULF breast MRI. Purpose-built ULF systems could support different imaging orientations (such as supine, sitting, or standing) and innovative magnet designs may improve portability and reduce overall system complexity. Such engineering advances could enable use in settings where conventional high-field MRI systems (1.5 T and 3 T) are impractical.

Given these possibilities, ULF MRI may ultimately broaden the contexts in which breast imaging can be performed. However, establishing any clinical role, whether for screening, diagnostic evaluation, or monitoring, will require substantial further work. This includes systematic studies assessing image quality across larger cohorts, evaluations in patients with benign and malignant lesions, and investigations of contrast-enhanced protocols.

In summary, our demonstration of ULF breast MRI represents an early technical step. Future research will be essential to determine the diagnostic performance, practicality, and potential clinical applications of ULF breast imaging.

Methods

Study design

This prospective pilot study was performed to observe the capabilities of breast imaging at 6.5 mT. The observational study was granted institutional review board approval from the Office for Human Research Studies (protocol 21-579) at the Dana-Farber/Harvard Cancer Center. All methods were performed in accordance with the relevant guidelines and regulations. Written informed consent was obtained from each participant.

11 healthy female participants (mean age, 35 years \pm 13 years), two patients with a history of breast cancer (ages 51 and 58 years, respectively), and one 48-year-old patient with a benign mass were enrolled. Exclusion criteria were: pregnancy, breastfeeding, or inability to undergo MRI due to presence of an implanted or external MRI unsafe device or MR conditional device not meeting the conditions required for the scan. Participants had to be older than 20 and younger than 80 years old. The study also excluded individuals directly supervised by study investigators.

Imaging system

Imaging was performed on a custom-built electromagnetic MRI scanner, shown in Fig. 1A and previously described⁵⁰. The scanner operates at a main field strength of 6.5 mT (Larmor frequency of 276.18 kHz). The magnetic field inhomogeneity measured over a 20 cm spherical region at isocenter is less than 10 Hz following shimming on a spherical phantom. Imaging gradients are produced by a biplanar gradient set capable of producing linear gradients of up to 1 mT/m in all three axes. Prior to all acquisitions, active shimming is provided using the gradient system.

For this study, the imaging bed was modified from its previous configuration for neuroimaging⁵⁰ to a breast imaging setup where the breast and dedicated RF coil are located at the isocenter of the scanner. Figure 1B–D illustrates the imaging bed and dedicated RF coil designed to image a single breast. In order to achieve a good filling factor and thus a high SNR⁵⁷, a close-fitting conical breast RF coil was designed. The RF coil design was determined based on several factors. The conical geometry was based on promising study results at higher field strengths⁵⁸ and adapted in size to enable imaging of larger breasts, using reported common breast sizes in the U.S. as a reference⁵⁹. The coil height is 10 cm; its diameter at the base is 19 cm; and its diameter at the peak is 4 cm^{60–62}. The RF coil was uniformly wound on a conical supporting structure, with all grooves populated to ensure an evenly distributed winding pattern. Along the conical surface, there are 20 wire turns distributed at

one turn per groove, and the end plate contains 3 wire turns. This design allows coverage of the entire breast and the chest wall up to a depth of approximately 3 cm (Fig. 1C).

The RF magnetic field was calculated using the Finite-Element-Method simulation (Ansys Maxwell, 2021, Ansys, Canonsburg, PA, USA). The simulated magnetic field was used to assess the field homogeneity within the breast volume and to determine the magnetic field fall-off beyond the physical end of the coil. The resultant field map (Fig. 1E) revealed a field inhomogeneity of approximately $\pm 60\%$ across the breast volume and a magnetic field fall-off of 30% within 3 cm beyond the chest wall.

To evaluate coil homogeneity and sensitivity, a homogeneous flexible phantom consisting of a latex balloon filled with deionized water was positioned inside the coil and scanned. This MR phantom was placed inside the breast RF coil, and as seen in Fig. 1F, it occupied the entire imaging region-of-interest (Fig. 1F). The imaging protocol used to scan the MR phantom was the same as that of participant scanning protocol. The resulting phantom MR image (Fig. 1G) demonstrated high sensitivity within the coil and a marked decrease towards the coil opening, consistent with the simulated field distribution.

MRI acquisition

An axial 3D balanced steady-state free precession (bSSFP) sequence was used in this study with a flip angle of 70° , TE (echo time)/TR (repetition time) of 13 ms/26 ms, a matrix size of $64 \times 72 \times 21$ (21 slices) and 50 averages. To accelerate the imaging process, an under-sampling factor of 70% was used. Depending on the evaluation criteria, for all healthy participants the left breast was scanned with a voxel size of $3 \text{ mm} \times 3 \text{ mm} \times 8 \text{ mm}$, resulting in 21 slices and a total scan time was 21 min 36 s. For the three patients with either breast cancer history or benign mass, the spatial resolution and FOV was adjusted depending on the size of the breast, but the number of slices remained fixed at 21. The patient with a history of invasive ductal carcinoma and papillary carcinoma in the subareolar region of the right breast was scanned for 30 min with a spatial resolution of $2 \text{ mm} \times 2 \text{ mm} \times 6 \text{ mm}$ (21 slices). The patient with a history of invasive lobular carcinoma and the patient with a cystic mass in their left breasts were scanned for 45 min with a spatial resolution of $2 \text{ mm} \times 2 \text{ mm} \times 4 \text{ mm}$ (21 slices). Given the scan duration, the study was limited to imaging one breast. No contrast agents were used.

Images were reconstructed in MATLAB (Natick, MA, USA) using inverse fast Fourier transform (IFFT) with the under-sampled region zero-filled in k-space. Images were converted into DICOM format using the MATLAB function `dicomwrite`. No data-driven artificial intelligence (AI) or other machine learning-based methods were used in the image acquisition or reconstruction.

The images of all 11 healthy participants were reviewed by three board-certified breast radiologists (M.A.S., L.R.L., and J.C.V.C.) with 13, 9, and 3 years of experience reading breast MRI. The readers reviewed the evaluation criteria; however, due to the limited data of this pilot study, no additional images were used to train the readers. Images were viewed in DICOM format using 3D Slicer⁶³. The visibility of the following features in the breast was assessed: visibility of the breast outline, visibility of the FGT compared to intramammary adipose tissue, demarcation of the NAC, and visualization of the pectoralis muscle (chest wall). Visibility of these features was assessed using a 5-point Likert scale (1—not at all visible, 2—barely visible, 3—clearly visible but blurred, 4—clearly visible and sharp, 5—clearly visible and very sharp). Breast density was assessed qualitatively by the breast radiologists. Fibroglandular tissue (FGT) patterns were categorized as fatty, scattered, heterogeneous, or extreme. These categories correspond directly to the American College of Radiology BI-RADS breast density classification system (categories A–D). Images were also evaluated for motion artifacts.

Three of the 11 healthy participants had screening mammograms available for comparison to the ULF MRI. The screening mammograms were reviewed by one board-certified radiologist (M.A.S.) with 13 years of experience with breast MRI. The radiologist noted the breast tissue pattern and visibility of key breast features on the ULF MRI and the x-ray mammogram.

For the three patients with either breast cancer history or benign mass, the ULF MRI and any clinical imaging were reviewed by one board-certified radiologist (M.A.S.) with 13 years of experience with breast MRI. The radiologist noted the breast tissue pattern, visibility of key breast features, and any clinical findings across all images.

Statistical analysis

Inter-reader agreement was assessed by computing Fleiss' kappa among three readers' feature visibility assessments. In this study, the primary objective was to determine whether breast tissue structures could be identified. To achieve this, we introduced a five-point scoring system for image quality in the reader study, where a score of 1 indicated non-visibility and scores of 2–5 represented increasing degrees of visibility. For data analysis, the scores were grouped into two categories, with a score of 1 classified as non-visible and scores of 2–5 classified as visible, in order to directly address the primary objective.

Due to the novelty of these images, and the limited dataset, which did not allow for proper training or calibration, inter-observer variability was observed across readers. Consequently, the five-point scale was revised to a binary scale for statistical analysis, assessing whether or not a feature was visible (1—not at all visible, 2 or greater—visible). All statistical analyses were performed using IBM SPSS Statistics for Windows, version 26.0 (IBM Corp., Armonk, NY, USA). The original five-point scoring data are presented for completeness, but no further statistical analyses of these ordinal ratings were performed, as such analyses would not significantly affect the study's conclusions.

Data availability

All data generated or analyzed during the study are available in the main text.

Received: 12 June 2025; Accepted: 20 January 2026

References

1. United Nations Department of Economic & Social Affairs Population Division. *World Population Prospects 2024, Online Edition* (2024). Preprint at <https://population.un.org/wpp/>.
2. Global Burden of Disease Collaborative Network. *Global Burden of Disease Study 2021 (GBD 2021) Results*. Seattle, United States: Institute for Health Metrics and Evaluation (IHME) (2022). <https://vizhub.healthdata.org/gbd-results/>.
3. Howlander, N., Noone, A., Krapcho, M. et al. *SEER Cancer Statistics Review, 1975–2017. Table 4.17. Cancer of the Female Breast (Invasive)-Lifetime Risk of Being Diagnosed with Cancer given Alive and Cancer-Free at Current Age* (National Cancer Institute, Bethesda).
4. Haber, G., Ahmed, N. U. & Pekovic, V. Family history of cancer and its association with breast cancer risk perception and repeat mammography. *Am. J. Public Health* **102**, 2322–2329 (2012).
5. Gao, Y., Samreen, N. & Heller, S. L. Non-*BRCA* early-onset breast cancer in young women. *Radiographics* **42**, 5–22 (2022).
6. Kehm, R. D., Daaboul, J. M., Tehranifar, P. & Terry, M. B. Geographic differences in early-onset breast cancer incidence trends in the USA, 2001–2020, is it time for a geographic risk score?. *Cancer Causes Control* <https://doi.org/10.1007/s10552-025-01968-7> (2025).
7. Lima, S. M., Kehm, R. D. & Terry, M. B. Global breast cancer incidence and mortality trends by region, age-groups, and fertility patterns. *EClinicalMedicine* **38**, 100985 (2021).
8. Payne, J. I., Martin, T., Caines, J. S. & Duggan, R. The burden of false-positive results in analog and digital screening mammography: Experience of the Nova Scotia breast screening program. *Can. Assoc. Radiol. J.* **65**, 315–320 (2014).
9. Smith-Bindman, R. Comparison of screening mammography in the United States and the United Kingdom. *JAMA* **290**, 2129 (2003).
10. Le, M. T., Mothersill, C. E., Seymour, C. B. & McNeill, F. E. Is the false-positive rate in mammography in North America too high?. *Br. J. Radiol.* **89**, 20160045 (2016).
11. Lamb, L. R., Mohallem Fonseca, M., Verma, R. & Seely, J. M. Missed breast cancer: Effects of subconscious bias and lesion characteristics. *Radiographics* **40**, 941–960 (2020).
12. Moberg, K. et al. Two models for radiological reviewing of interval cancers. *J. Med. Screen.* **6**, 35–39 (1999).
13. Ciatto, S. et al. Interval breast cancers in screening: The effect of mammography review method on classification. *Breast* **16**, 646–652 (2007).
14. Hofvind, S. et al. Influence of review design on percentages of missed interval breast cancers: Retrospective study of interval cancers in a population-based screening program. *Radiology* **237**, 437–443 (2005).
15. Van Dijk, J. A. A. M., Verbeek, A. L. M., Hendriks, J. H. C. L. & Holland, R. The current detectability of breast cancer in a mammographic screening program. A review of the previous mammograms of interval and screen-detected cancers. *Cancer* **72**, 1933–1938 (1993).
16. Hoff, S. R. et al. Missed and true interval and screen-detected breast cancers in a population based screening program. *Acad. Radiol.* **18**, 454–460 (2011).
17. National Breast Cancer Coalition. *Mammography for Breast Cancer Screening: Harm/Benefit Analysis* (2021). <https://www.stopbreastcancer.org/information-center/positionspolicies/mammography-for-breast-cancer-screening-harm-benefit-analysis/>.
18. National Center for Health Statistics. *Health, United States, 2018: Table 33: Use of Mammography among Women Aged 40 and over, by Selected Characteristics: United States, Selected Years 1987–2015* (2018).
19. Organization, W. H. *WHO Position Paper on Mammography Screening* (2021).
20. Mann, R. M., Cho, N. & Moy, L. Breast MRI: State of the Art. *Radiology* **292**, 520–536 (2019).
21. Mann, R. M. et al. Breast MRI: EUSOBI recommendations for women's information. *Eur. Radiol.* **25**, 3669–3678 (2015).
22. Saslow, D. et al. American Cancer Society guidelines for breast screening with MRI as an adjunct to mammography. *CA Cancer J. Clin.* **57**, 75–89 (2007).
23. Monticciolo, D. L., Newell, M. S., Moy, L., Lee, C. S. & Destounis, S. V. Breast cancer screening for women at higher-than-average risk: Updated recommendations from the ACR. *J. Am. Coll. Radiol.* <https://doi.org/10.1016/j.jacr.2023.04.002> (2023).
24. Yamaguchi, K. et al. Breast cancer detected on an incident (second or subsequent) round of screening MRI: MRI features of false-negative cases. *Am. J. Roentgenol.* **201**, 1155–1163 (2013).
25. Vreemann, S. et al. The frequency of missed breast cancers in women participating in a high-risk MRI screening program. *Breast Cancer Res. Treat.* **169**, 323–331 (2018).
26. Montemurro, F. et al. Relationship between DCE-MRI morphological and functional features and histopathological characteristics of breast cancer. *Eur. Radiol.* **17**, 1490–1497 (2007).
27. Tan, S. L. L. et al. Differentiation between benign and malignant breast lesions using quantitative diffusion-weighted sequence on 3 T MRI. *Clin. Radiol.* **69**, 63–71 (2014).
28. Partridge, S. C. et al. Diffusion-weighted MRI findings predict pathologic response in neoadjuvant treatment of breast cancer: The ACRIN 6698 multicenter trial. *Radiology* **289**, 618–627 (2018).
29. Miles, R. et al. Underutilization of supplemental magnetic resonance imaging screening among patients at high breast cancer risk. *J. Womens Health* **27**, 748–754 (2018).
30. Comstock, C. E. et al. Comparison of abbreviated breast MRI vs digital breast tomosynthesis for breast cancer detection among women with dense breasts undergoing screening. *JAMA* **323**, 746–756 (2020).
31. Abate, F. et al. UNITY: A low-field magnetic resonance neuroimaging initiative to characterize neurodevelopment in low and middle-income settings. *Dev. Cogn. Neurosci.* **69**, 101397 (2024).
32. Kimberly, W. T. et al. Brain imaging with portable low-field MRI. *Nat. Rev. Bioeng.* <https://doi.org/10.1038/s44222-023-00086-w> (2023).
33. Yuen, M. M. et al. Portable, low-field magnetic resonance imaging enables highly accessible and dynamic bedside evaluation of ischemic stroke. *Sci. Adv.* **8**, eabm3952 (2022).
34. Mazurek, M. H. et al. Portable, bedside, low-field magnetic resonance imaging for evaluation of intracerebral hemorrhage. *Nat. Commun.* **12**, 5119 (2021).
35. Sheth, K. N. et al. Assessment of brain injury using portable, low-field magnetic resonance imaging at the bedside of critically ill patients. *JAMA Neurol.* **78**, 41 (2021).
36. Prabhat, A. M. et al. Methodology for low-field, portable magnetic resonance neuroimaging at the bedside. *Front. Neurol.* **12**, 760321 (2021).
37. de Havenon, A. et al. Identification of white matter hyperintensities in routine emergency department visits using portable bedside magnetic resonance imaging. *J. Am. Heart Assoc.* **12**, e029242 (2023).
38. Medina, D. et al. Nuclear magnetic resonance studies on human breast dysplasias and neoplasms. *J. Natl. Cancer Inst.* **54**, 813–818 (1975).
39. Mansfield, P. et al. Carcinoma of the breast imaged by nuclear magnetic resonance (NMR). *Br. J. Radiol.* **52**, 242–243 (1979).
40. Mansfield, P. et al. Human whole body imaging and detection of breast tumours by NMR. *Philos. Trans. R. Soc. Lond. B Biol. Sci.* **289**, 503–510 (1980).

41. Ross, R. J., Thompson, J. S., Kim, K. & Bailey, R. A. Nuclear magnetic resonance imaging and evaluation of human breast tissue: Preliminary clinical trials. *Radiology* **143**, 195–205 (1982).
42. Koenig, S. H. & Brown, R. D. III. Determinants of proton relaxation rates in tissue. *Magn. Reson. Med.* **1**, 437–449 (1984).
43. Bitonto, V. et al. Low-field NMR relaxometry for intraoperative tumour margin assessment in breast-conserving surgery. *Cancers (Basel)* **13**, 4141 (2021).
44. Howlader, N., Noone, A., Krapcho, M. et al. *SEER Cancer Statistics Review, 1975–2017. Table 4.17. Cancer of the Female Breast (Invasive)-Lifetime Risk of Being Diagnosed with Cancer given Alive and Cancer-Free at Current Age* (National Cancer Institute, Bethesda). http://seer.cancer.gov/csr/1975_2017/.
45. Ilic, I. & Ilic, M. International patterns and trends in the brain cancer incidence and mortality: An observational study based on the global burden of disease. *Heliyon* **9**, e18222 (2023).
46. Dewan, M. C. et al. Estimating the global incidence of traumatic brain injury. *J. Neurosurg.* **130**, 1080–1097 (2019).
47. James, S. L. et al. Global, regional, and national burden of traumatic brain injury and spinal cord injury, 1990–2016: A systematic analysis for the Global Burden of Disease Study 2016. *Lancet Neurol.* **18**, 56–87 (2019).
48. Organization, W. S. *Global Stroke Fact Sheet 2022* (2022).
49. Bottomley, P. A., Foster, T. H., Argersinger, R. E. & Pfeifer, L. M. A review of normal tissue hydrogen NMR relaxation times and relaxation mechanisms from 1 to 100 MHz: Dependence on tissue type, NMR frequency, temperature, species, excision, and age. *Med. Phys.* **11**, 425–448 (1984).
50. Sarracanie, M. et al. Low-cost high-performance MRI. *Sci. Rep.* **5**, 15177 (2015).
51. Kremser, C. et al. Quantification of breast biopsy clip marker artifact on routine breast MRI sequences: A phantom study. *Eur. Radiol. Exp.* **8**, 128 (2024).
52. Genson, C. C., Blane, C. E., Helvie, M. A., Waits, S. A. & Chenevert, T. L. Effects on breast MRI of artifacts caused by metallic tissue marker clips. *Am. J. Roentgenol.* **188**, 372–376 (2007).
53. American College of Radiology. *MRI Exam-Specific Parameters: Breast* (2025). <https://accreditation.support.acr.org/support/solutions/articles/11000114407-mri-exam-specific-parameters-breast-revised-3-19-2025-%5C>. Revised 19 March 2025.
54. Koonjoo, N., Hornung, T. P. P., Susu, Y., Rosen, M. S. & Bortfeld, T. R. Low field Breast and chest wall imaging for MR guided proton therapy. In *Proceedings of the 31st Annual Meeting and Exhibition of the International Society for Magnetic Resonance in Medicine (ISMRM)* Program Number 3895 (Toronto, Canada, 2023).
55. Komu, M. & Korman, M. Breast coil design for low-field MRI. *Magn. Reson. Med.* **27**, 165–170 (1992).
56. Hoult, D. I. & Richards, R. E. The signal-to-noise ratio of the nuclear magnetic resonance experiment. *J. Magn. Reson.* **1969**(24), 71–85 (1976).
57. Shen, S., Xu, Z., Koonjoo, N. & Rosen, M. S. Optimization of a close-fitting volume RF coil for brain imaging at 6.5 mT using linear programming. *IEEE Trans. Biomed. Eng.* **68**, 1106–1114 (2021).
58. Sun, L., Olsen, J. O. & Robitaille, P.-M.L. Design and optimization of a breast coil for magnetic resonance imaging. *Magn. Reson. Imaging* **11**, 73–80 (1993).
59. Eriksson, N. et al. Genetic variants associated with breast size also influence breast cancer risk. *BMC Med. Genet.* **13**, 53 (2012).
60. Hornung, T. P. P., Koonjoo, N., Susu, Y., Rosen, M. S. & Bortfeld, T. R. Breast and chest RF design and optimization for ultra-low field MRI. In *Proceedings of the 31st Annual Meeting and Exhibition of the International Society for Magnetic Resonance in Medicine (ISMRM)* program number 1772 (Toronto, Canada, 2023).
61. Koonjoo, N., Hornung, T. P. P., Susu, Y., Rosen, M. S. & Bortfeld, T. R. Low field breast and chest wall imaging for MR guided proton Therapy. In *Proceedings of the 31st Annual Meeting & Exhibition of the International Society for Magnetic Resonance in Medicine (ISMRM)* Program Number 3895 (Toronto, Canada, 2023).
62. Hornung, T. P. P. et al. Breast coil optimization for low field MRI and future MR-guided proton therapy. *IEEE Trans. Biomed. Eng.* **72**, 1750–1765 (2025).
63. Fedorov, A. et al. 3D Slicer as an image computing platform for the quantitative imaging network. *Magn. Reson. Imaging* **30**, 1323–1341 (2012).

Acknowledgements

The authors would like to thank Darrah Bowden for her invaluable assistance and perspective on the breast imaging configuration. They also extend their sincere thanks to Dr. Sarah M. Friedewald, MD, and Ellie Friedewald for their support of this low-field breast work. M.S.R dedicates this work to the memory of Christina Pfeifer Mattig.

NIST Disclaimer

Certain commercial equipment, instruments, or materials are identified in this paper in order to specify the experimental procedure adequately. Such identification is not intended to imply recommendation or endorsement by NIST, nor is it intended to imply that the materials or equipment identified are necessarily the best available for the purpose.

Author contributions

Conceptualization: K.E.K, M.S.R Methodology: S.S, N.K, F.K.L, M.A.S, T.P.P.H, S.E.O Investigation: S.S, N.K, F.K.L, M.A.S, L.R.L, J.V.C.V, T.P.P.H, M.S.R Visualization: S.S, N.K, M.A.S, L.R.L, J.V.C.V, S.E.O, K.E.K, M.S.R Supervision: S.Y, T.R.B, K.E.K, M.A.S, M.S.R Writing—original draft: S.S, N.K, K.E.K, M.S.R Writing—review and editing: S.S, N.K, F.K.L, M.A.S, L.R.L, J.V.C.V, T.P.P.H, S.E.O, S.Y, T.R.B, K.E.K, M.S.R

Funding

National Institutes of Health grant 1R21CA267315 (KEK, MSR). Kiyomi and Ed Baird MGH Research Scholar award (MSR). German-American Fulbright Commission (FKL). National Institute of Standards and Technology (KEK, SEO). NIST-PREP 70NANB18H006 from U.S. Department of Commerce (SEO).

Declarations

Competing interests

MSR is a founder and equity holder of Hyperfine, Inc. MSR is a/ppconsultant and equity holder in DeepSpin GmbH. All other authors declare no conflicts.

Additional information

Supplementary Information The online version contains supplementary material available at <https://doi.org/10.1038/s41598-026-37130-9>.

Correspondence and requests for materials should be addressed to M.S.R.

Reprints and permissions information is available at www.nature.com/reprints.

Publisher's note Springer Nature remains neutral with regard to jurisdictional claims in published maps and institutional affiliations.

Open Access This article is licensed under a Creative Commons Attribution-NonCommercial-NoDerivatives 4.0 International License, which permits any non-commercial use, sharing, distribution and reproduction in any medium or format, as long as you give appropriate credit to the original author(s) and the source, provide a link to the Creative Commons licence, and indicate if you modified the licensed material. You do not have permission under this licence to share adapted material derived from this article or parts of it. The images or other third party material in this article are included in the article's Creative Commons licence, unless indicated otherwise in a credit line to the material. If material is not included in the article's Creative Commons licence and your intended use is not permitted by statutory regulation or exceeds the permitted use, you will need to obtain permission directly from the copyright holder. To view a copy of this licence, visit <http://creativecommons.org/licenses/by-nc-nd/4.0/>.

© The Author(s) 2026